ACS Catalysis

pubs.acs.org/acscatalysis Research Article

Empowering Catalyst Supports: A New Concept for Catalyst Design Demonstrated in the Fischer–Tropsch Synthesis

Motlokoa Khasu, Wijnand Marquart, Patricia J. Kooyman, Charalampos Drivas, Mark A. Isaacs, Alexander J. Mayer, Sandie E. Dann, Simon A. Kondrat, Michael Claeys, and Nico Fischer*

Cite This: *ACS Catal.* 2023, 13, 6862–6872 Read Online

ACCESS | Metrics & More | Article Recommendations | Supporting Information

ABSTRACT: The Fischer–Tropsch (FT) synthesis is traditionally associated with fossil fuel consumption, but recently this technology has emerged as a keystone that enables the conversion of captured CO_2 with sustainable hydrogen to energy-dense fuels and chemicals for sectors which are challenging to be electrified. Iron-based FT catalysts are promoted with alkali and transition metals to improve reducibility, activity, and selectivity. Due to their low concentration and the metastable state under reaction conditions, the exact speciation and location of these promoters remain poorly understood. We now show that the selectivity promoters such as potassium and manganese, locked into an oxidic matrix doubling as a catalyst support, surpass conventional promoting effects. $La_{1-x}K_xAl_{1-y}Mn_yO_{3-\delta}$ (x = 0 or 0.1; y = 0, 0.2, 0.6, or 1) perovskite supports yield a 60% increase in CO conversion comparable to conventional promotion but show reduced CO_2 and overall C_1 selectivity. The presented approach to promotion seems to decouple the enhancement of the FT and the water–gas shift reaction. We introduce a general catalyst design principle that can be extended to other key catalytic processes relying on alkali and transition metal promotion.

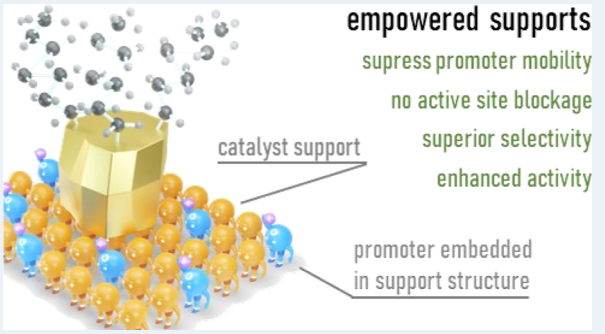

KEYWORDS: *iron-based Fischer–Tropsch synthesis, potassium promotion, manganese promotion, perovskite supports, novel promoter delivery*

INTRODUCTION

Potassium and manganese are commonly included in iron-based Fischer–Tropsch (FT) catalysts as promoters *via* impregnation or precipitation.[1] The effect of the alkali promotion on the catalytic performance is based on a modification of the local electron density of the active iron phase.[2] This results in stronger CO adsorption on the catalyst, weakening of the C–O bond, and decreased dissociative adsorption of H_2. Conventionally, the FT activity increases up to a maximum K concentration upon which further improvement is hindered due to site blockage by the promoter itself or by enhanced C deposits.[3,4] In the presence of K, the product spectrum of the FT synthesis increases in value with a higher olefin content, an overall increased chain growth probability, and a reduced methane selectivity.[5] Concomitantly, an increased water–gas shift (WGS) activity[6,7] has been reported, aiding in the conversion of hydrogen-lean synthesis gas feeds obtained from the gasification of coal or biomass. Manganese promotion increases the number of basic sites while reducing their strength, further enhancing chain growth probability and olefin selectivity, especially at lower hydrocarbon chain lengths.[8,9] Particles of manganese oxide forming under reaction conditions have further been shown to suppress sintering of the active iron phase.[10]

The exact speciation of promoter elements under reaction conditions[11] is still not fully resolved. Low concentrations and promoter mobility[4,12] present the most significant challenges in this regard. Without a clear understanding of the interaction between the promoter and the active phase, catalyst optimization through rational design is not possible. Innovative preparation techniques have shown that when an intimate contact between the active phase and the promoter is achieved, the promoting effects observed surpass effects reported for catalysts prepared with conventional impregnation approaches.[13]

We have now developed a doped $LaAlO_3$-based perovskite of general formula, ABO_3, with K (10 at. %) partially replacing La on the A site and Mn (20–100 at. %) replacing Al on the B site which serves as a support for pre-prepared γ-Fe_2O_3 nanoparticles. These catalysts are employed for low-temperature slurry-based FT synthesis. The samples with partial

Received: February 28, 2023
Revised: April 10, 2023

substitution of lanthanum with potassium display a 60% higher CO conversion, matching the performance enhancement achieved through conventional impregnation of 0.5 and 1 wt % K. However, our new catalysts do not enhance the WGS activity to the same extent and therefore have, at a comparable methane selectivity, an overall lower undesired C_1 product selectivity. The addition of small amounts of Mn to the crystal lattice of the perovskite further increases the chain growth probability at a stable olefin content.

EXPERIMENTAL SECTION

Synthesis of Perovskites. $La_{1-x}K_xAl_{1-y}Mn_yO_{3-\delta}$ with x = 0 or 0.1 and y = 0, 0.2, 0.6, or 1 was prepared *via* the citrate sol−gel autocombustion method.[14] $La(NO_3)_2{\cdot}6H_2O$ ($(1-x) \times 5.75$ mmol), KNO_3 ($x \times 5.75$ mmol), $Al(NO_3)_3{\cdot}9H_2O$ ($(1-y) \times 5.75$ mmol), and $Mn(NO_3)_2{\cdot}4H_2O$ ($y \times 5.75$ mmol) were dissolved in deionized water (150 mL). Citric acid monohydrate (4.83 g, 23.0 mmol) and concentrated nitric acid (15.8 M, 1.5 mL, 23.7 mmol) were added in an acid to metal cation molar ratio of 2.0:1 and 2.1:1, respectively. After full dissolution at 60 °C, ethylene glycol (2.1 g, 1.9 mL, 34.5 mmol) was added and the mixture was heated to 90 °C for 1 h. The solvent was evaporated at 100 °C, and the residual gel was heated to 350 °C to yield a black solid. This solid was collected, ground to a fine powder, and calcined in static air at 800 °C for 6 h.

Synthesis of γ-Fe_2O_3 Nanoparticles. Aqueous solutions of $FeCl_2{\cdot}4H_2O$ (0.25 M, 40 mL), NaOH (5.4 M, 40 mL), and NH_3 (1.34 M, 40 mL) were mixed and heated to 90 °C under nitrogen atmosphere for 90 min. The reaction mixture was cooled to 25 °C, and aqueous HCl (0.1 M, 40 mL) was added dropwise. The solid precipitate was collected by filtration, washed with H_2O (20 × 200 mL), and dried in air at 120 °C.

Deposition of γ-Fe_2O_3 Nanoparticles on Supports. Iron oxide nanoparticles (1.43 g, 9.0 mmol) were dispersed by sonication (1 h) in H_2O (500 mL). The solid support was added to the suspension to achieve a 20 wt % γ-Fe_2O_3 loading, and the reaction mixture was sonicated for an additional 1 h. The solvent was evaporated at 80 °C under reduced pressure (150 mbar), and the solid residue was dried in air at 120 °C for 12 h. In comparison, Al_2O_3 (Puralox SCCa 5-150, Sasol Technology), TiO_2 (P25, Evonik Industries), ZrO_2 (US Nano), and SiO_2 (Sigma-Aldrich) were used as model catalyst support materials. The commercial supports were dried at 300 °C for 5 h in air to remove residual moisture before being added to the suspension.

Impregnation with Potassium. $LaAlO_3$ (7.5 g, 35.1 mmol) and KNO_3 (0.5 wt % K, 37.5 mg, 0.37 mmol; 1.0 wt % K, 75.0 mg, 0.74 mmol; and 2.0 wt % K, 150.0 mg, 1.48 mmol) were dispersed in H_2O (100 mL). The solvent was evaporated at 80 °C under reduced pressure (150 mbar), and the solid residue was dried in air at 120 °C for 12 h. The powdered residue was heated in a fluidised bed glass reactor in an air stream to 350 °C at 2 °C·min^{-1} and held for 5 h.

Atomic Adsorption Spectroscopy. The elemental composition of the synthesised materials was determined using atomic adsorption spectroscopy. The sample (100 mg) was mixed with a HCl/HF mixture (10 mL at a 4:1 ratio) and brought to boil. Concentrated HNO_3 (10 mL) was added, and the volume of the liquid reduced to approximately 2 mL. $HClO_4$ (5 mL) was added, and the volume again reduced to approximately 2 mL. After cooling, the solution was diluted to 100 mL with distilled water and filtered before measurement in the Agilent 4200 MP-AES spectrometer.

Inductively Coupled Plasma Optical Emission Spectroscopy. The sample (100 mg) was dissolved in a mixture of concentrated aqueous HCl (3 mL), concentrated aqueous HF (3 mL), and concentrated aqueous HNO_3 (5−10 drops) and heated to 130 °C for 1 h using a microwave reactor. The reaction mixture was cooled to 24 °C. After cooling, 60 mL of H_3BO_3 was added. The analysis is conducted in a VARIAN OES-730 ICP−OES spectrometer.

Transition Electron Microscopy. The crystallite size distribution of the synthesised γ-Fe_2O_3 (maghemite) nanoparticles was extracted from micrographs collected in a Tecnai F20 transmission electron microscope equipped with a field emission gun, operated at 200 kV. Scanning transition electron microscopy (TEM) micrographs and elemental mapping *via* electron-dispersive spectrometry (EDS) were acquired using two different instruments. In one instance, a double aberration-corrected JEOL JEM-ARM 200F was used, operated at 200 kV, and equipped with an Oxford Xmax100 TLE EDS detector. Imaging and analysis of the samples were done in a scanning transmission electron microscopy (STEM) mode using a sub-angstrom-sized probe with a probe current between 68 and 281 pA. Probe current conditions were selected to optimise the beam current but, at the same time, to minimise the risk of beam damage to the specimen. The convergence semi-angle of the probe used was fixed at 23 mrad with acceptance semi-angles of the dark-field detector being 34 to 137 mrad. The bright-field (BF) detector acceptance semi-angle was set at 0 to 12 mrad by using an illumination limiting aperture. In the other instance, STEM BF, high-angle annular dark-field, and EDS elemental mapping were recorded using a ThermoFisher Tecnai Osiris, equipped with a FEG operated at 200 kV and four Bruker windowless SSD EDX detectors in the SuperX configuration. TEM samples were prepared by depositing a few drops of the sample suspended in ethanol onto a Quantifoil R1.2/1.3 carbon film on a copper grid followed by drying at room temperature.

X-ray Photoelectron Spectroscopy. X-ray photoelectron spectroscopy (XPS) data were acquired using a Kratos Axis SUPRA using monochromated Al kα (1486.69 eV) X-rays at 15 mA emission and 12 kV HT (180 W) and a spot size/analysis area of 700 × 300 μm. The instrument was calibrated to gold metal Au 4f (83.95 eV), and dispersion adjusted to give a BE of 932.6 eV for the Cu $2p_{3/2}$ line of metallic copper. Ag $3d_{5/2}$ line FWHM at 10 eV pass energy was 0.544 eV. Source resolution for monochromatic Al Kα X-rays is ∼0.3 eV. Using the Fermi edge of the valence band for metallic silver, the instrumental resolution was determined to be 0.29 at 10 eV pass energy (resolution with a charge compensation system on <1.33 eV FWHM on PTFE). High-resolution spectra were obtained using a pass energy of 40 eV, a step size of 0.1 eV, and a sweep time of 60 s, resulting in a line width of 0.696 eV for Au $4f_{7/2}$. Survey spectra were obtained using a pass energy of 160 eV. Charge neutralisation was achieved using an electron flood gun with a filament current of 0.45 A, a charge balance of 1 V, and a filament bias of 5 V. Successful neutralisation was adjudged by analysing the C 1s and Al 2p regions, wherein sharp peaks with no lower BE structure were obtained. Spectra have been charge-corrected to the main line of the carbon 1s spectrum (adventitious carbon) set to 284.8 eV. All data were recorded at a base pressure of below 9×10^{-9} Torr and a room temperature of 294 K. Data were analysed using CasaXPS

https://doi.org/10.1021/acscatal.3c00924
ACS Catal. 2023, 13, 6862−6872

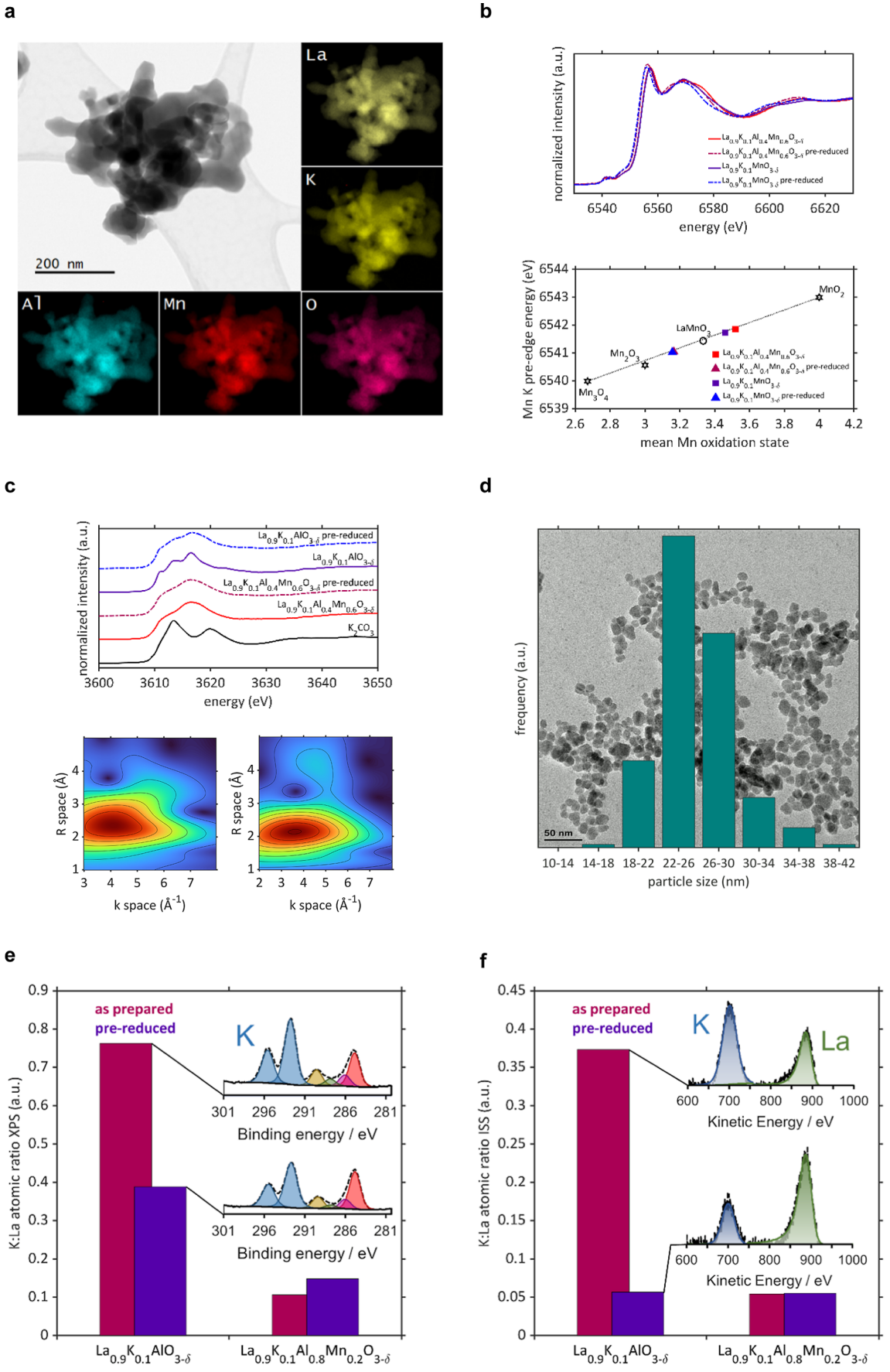

Figure 1. Structural characterization of perovskites. (a) Scanning transmission electron microscopy bright-field micrograph of $La_{0.9}K_{0.1}Al_{0.8}Mn_{0.2}O_{3-\delta}$ and individual electron-dispersive spectrometry maps of constituting elements. (b) Manganese K-edge X-ray absorption

https://doi.org/10.1021/acscatal.3c00924
ACS Catal. 2023, 13, 6862−6872

Figure 1. continued

near edge structure (XANES) spectra of $La_{0.9}K_{0.1}Al_{0.4}Mn_{0.6}O_{3-\delta}$ and $La_{0.9}K_{0.1}MnO_{3-\delta}$ as-prepared and after reductive pre-treatment (top) and manganese K pre-edge energies of $La_{0.9}K_{0.1}Al_{0.4}Mn_{0.6}O_{3-\delta}$ and $La_{0.9}K_{0.1}MnO_{3-\delta}$ as-prepared and after reductive pre-treatment as well as $LaMnO_3$, Mn_3O_4, Mn_2O_3, and MnO_2 literature[20] as a function of mean Mn-oxidation state (bottom). (c) Potassium K-edge XANES spectra of $La_{0.9}K_{0.1}Al_{0.4}Mn_{0.6}O_{3-\delta}$ and $La_{0.9}K_{0.1}AlO_{3-\delta}$ as-prepared and after reductive pre-treatment and of the K_2CO_3 reference (top) and wavelet transformation of k^1 weighted data from the potassium K-edge extended X-ray absorption fine structure spectra of K_2CO_3 (left bottom) and the pre-reduced $La_{0.9}K_{0.1}AlO_{3-\delta}$ (right bottom). (d) Particle size distribution of synthesised γ-Fe_2O_3 nanoparticles. (e) K/La atomic ratios from X-ray photoelectron spectroscopy analysis with (inset) K 2p + C 1s high-resolution spectra of as-prepared and pre-reduced $La_{0.9}K_{0.1}MnO_{3-\delta}$ (carbons: red = CC/CH, pink = C−O, green = C═O, yellow = carbonate/adsorbed CO_2). (f) K/La atomic ratios from ion scattering spectroscopy (ISS) (derived from calibration curve) with (inset) ISS spectra of as-prepared and pre-reduced $La_{0.9}K_{0.1}MnO_{3-\delta}$.

v2.3.26rev1.1 K. Peaks were fit with using Shirley background prior to component analysis, and symmetric peak functions (C 1s + K 2p) were modelled *via* nonlinear least-squared fitting using the line shape [La(1.53,243)].

Ion Scattering Spectroscopy. Ion scattering spectroscopy (ISS) data were acquired on a Kratos Axis SUPRA using a 1 keV He^+ ion beam (Minibeam 6 GCIS) rastered over an area of 1 × 1 mm and an electron flood gun charge neutraliser. Data were analysed using CasaXPS v2.3.26rev1.1 K. Asymmetric peak modelling was achieved using the line shape [LF-(1.21,8.45,200,83)], which was developed from the analysis of model reference materials, along with a peak area ratio calibration curve (La_2O_3, Sigma-Aldrich, 99% and KCl, Fisher Scientific, 99%).

X-ray Absorption Spectroscopy. X-ray absorption spectra (XAS) of the K and Mn K-edges were collected at beamline B-18 of the Diamond Light Source, UK. Access to the beamline was granted *via* the Block Allocation Group access managed by the UK Catalysis Hub. The perovskite samples investigated were exposed to a reducing atmosphere of flowing hydrogen (16 mL·min^{-1}·$g_{catalyst}^{-1}$), heated to 450 °C at 2 °C·min^{-1}, and held for 15 h to simulate the activation process in the FT catalytic process. The samples were deposited on a sticky Kapton film before XAS analysis. Data processing was performed using Athena from the Demeter software package.[15] To maximise the number of paths within the extended X-ray absorption fine structure (EXAFS) that could be fitted with the available potassium K-edge k space data, coordination numbers were fixed at appropriate values for the modelled structures, S_o^2 was fixed based on the fitting of KCl, and values $2\sigma^2$ were shared between suitable K−O paths. Both R_{factor} and reduced χ^2 fitting parameters are reported with the latter accounting for the quality for the fit with respect to the number of variables fitted.

X-ray Diffraction. Crystallite phase composition, structure, and size were probed using X-ray diffraction (XRD). All samples and precursors were analysed in a Bruker D8-ADVANCE diffractometer equipped with a Co source and a position sensitive detector (LYNXSEYE) operating in Bragg−Brentano geometry. For spent samples, the catalyst was first extracted from the FT wax *via* Soxhlet extraction with xylene. Selected samples were studied in an in-house developed in situ capillary stage[16] fitted to a Bruker D8-ADVANCE diffractometer equipped with a Mo source and a position sensitive detector (Vantec) operating in a parallel beam mode. The samples were heated in a continuous flow of H_2 at atmospheric pressure (40 mL·min^{-1}·$g_{catalyst}^{-1}$) from 50 to 450 °C at 2 °C·min^{-1} and held for 15 h. Subsequently, the temperature was reduced to 240 °C, the pressure increased to 13.5 bar, and the catalyst exposed for 250 min to a stream of H_2 and CO in a 2:1 ratio at a space velocity of 383 mL·min^{-1}·$g_{catalyst}^{-1}$. To achieve high temporal resolution in the in situ experiments, the scan range was limited to $1/d$ = 0.2948 to 0.6583 Å^{-1}, resulting in a scan time of below 5 min. All patterns were evaluated against the International Centre of Diffraction PDF-4+ database (release 2020), and quantitative analysis was performed using Rietveld refinement methodologies[17] incorporated in the TOPAS 5 (BRUKER) software package.

Catalytic Performance Evaluation. The activity and selectivity of all catalyst were evaluated in a 600 mL slurry-based continuous stirred tank reactor (CSTR). The catalyst (5 g) was reduced in hydrogen (16 mL·min^{-1}·$g_{catalyst}^{-1}$) in a glass reactor positioned in a vertical tubular furnace in a hydrogen flow. The reactor was heated to 450 °C at 2 °C·min^{-1} and held for 15 h. The sample was then cooled to room temperature in a flow of Ar and quickly transferred into 50 g of molten wax (Sasol H), which was also protected from air exposure with a blanket of Ar. The wax tablet containing the catalyst was added to 300 g of wax in the CSTR, already molten at 140 °C. The reactor was subsequently sealed, pressurised with argon to 15 bar at a stirring speed of 300 rpm, and heated to the reaction temperature of 240 °C. A synthesis gas mixture (H_2/CO = 2) with 10 vol % N_2 as an internal standard was fed to the reactor at 8 or 30 mL·min^{-1}·$g_{catalyst}^{-1}$ to start the FT synthesis. All permanent gases were continuously analysed using a gas chromatograph equipped with a thermal conductivity detector (Agilent 7820A). The hydrocarbon products were collected in pre-evacuated ampoules[18] and analysed using a gas chromatograph equipped with a flame ionization detector (Varian CP-3800). The methane signal was used to link the two chromatography data sets.

RESULTS AND DISCUSSION

A series of $La_{1-x}K_xAl_{1-y}Mn_yO_{3-\delta}$ with x = 0 or 0.1 and y = 0, 0.2, 0.6, or 1 were prepared *via* the citrate method. The content of substituents was somewhat lower than that targeted (Supporting Information Table S1), with the perovskite forming a single rhombohedral ($R\bar{3}c$) crystalline phase characteristic for lanthanum aluminate (Supporting Information Figure S1a). Good evidence to support the proposed substitution is given by increases in the a and c lattice parameters from 5.37 to 5.50 and 13.11 to 13.31 Å, respectively, as the amount of manganese increases due to the larger atomic radius of Mn^{3+} (0.580 Å) compared with Al^3 (0.535 Å) (Supporting Information Figure S1b). The BET surface area of the promoter-free perovskite is 5 m^2 g^{-1}. The incorporation of potassium increases the surface area to 29 m^2 g^{-1}, with the further addition of manganese reducing it gradually to 11 m^2 g^{-1}. No apparent surface enrichment of K or Mn is observed in energy-dispersive X-ray spectroscopy scanning electron microscopy (EDS−STEM) (Figure 1a, Supporting Information Figure S2 for higher magnification).

https://doi.org/10.1021/acscatal.3c00924
ACS Catal. 2023, 13, 6862−6872

Table 1. Manganese K-Edge EXAFS Fitting Values for $La_{0.9}K_{0.1}Al_{1-y}Mn_yO_{3-\delta}$ Perovskite Supports[a]

sample	scattering path	coordination number[b]	$2\sigma^2$ (Å^2)	R (Å)	delr	E_f (eV)	R_{factor}, reduced χ^2[c]
$LaMnO_3$ standard	Mn−O	6	0.007(1)	1.925(8)	−0.076(8)	−4(1)	0.0083 (486.8)
	Mn−La (a)	2	0.0021(18)	3.22(2)	−0.21(2)		
	Mn−La (b)	6	0.004(1)	3.36(1)	0.05(1)		
	Mn−Mn	6	0.014(2)	4.00(2)	−0.06(2)		
$La_{0.9}K_{0.1}Al_{0.4}Mn_{0.6}O_{3-\delta}$ pre-reduced	Mn−O	5.4(8)	0.0076(7)	1.92(1)	−0.09(1)	−8(2)	0.014 (452.2)
	Mn−La (a)	2	0.006(2)	3.17(5)	−0.26(5)		
	Mn−La (b)	6	0.005(2)	3.33(3)	−0.10(3)		
	Mn−Mn	6	0.011(5)	3.67(4)	−0.29(4)		
$La_{0.9}K_{0.1}Al_{0.4}Mn_{0.6}O_{3-\delta}$	Mn−O	6(1)	0.007(2)	1.89(1)	−0.11(1)	−6(2)	0.026 (731.0)
	Mn−La (a)	2	0.005[c]	3.20(7)	−0.22(7)		
	Mn−La (b)	6	0.005(1)	3.33(3)	−0.09(3)		
	Mn−Mn	6	0.014(5)	3.66(6)	−0.29(6)		
$La_{0.9}K_{0.1}MnO_{3-\delta}$ pre-reduced	Mn−O	5.0(5)	0.007(1)	1.928(9)	−0.072(9)	−5(1)	0.012 (214.0)
	Mn−La (a)	2	0.004(1)	3.22(2)	−0.21(2)		
	Mn−La (b)	6	0.0061(8)	3.37(1)	−0.06(1)		
	Mn−Mn	6	0.028(8)	4.08(5)	0.13(5)		
$La_{0.9}K_{0.1}MnO_{3-\delta}$	Mn−O	5.4(5)	0.006(1)	1.908(8)	−0.092(8)	−3(1)	0.0099 (616.1)
	Mn−La (a)	2	0.005(3)	3.23(3)	−0.19(3)		
	Mn−La (b)	6	0.005(1)	3.37(1)	−0.06(1)		
	Mn−Mn	6	0.017(3)	3.98(2)	0.03(2)		

[a]Fixed parameters: $S_o^2 = 0.71$, calculated from $LaMnO_3$ standard. [b]Coordination number fixed apart from Mn−O path. [c]Value given in brackets.

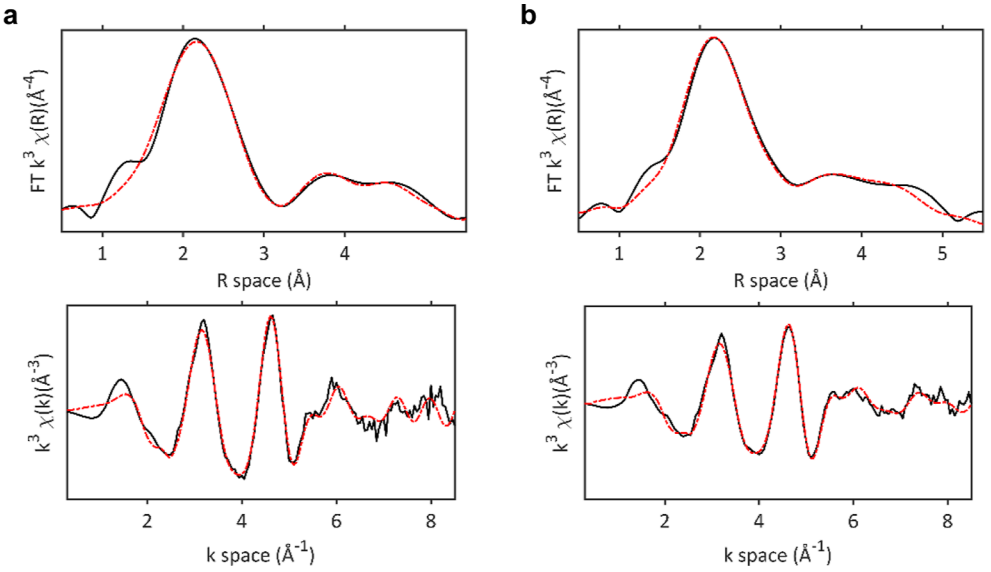

Figure 2. Potassium K-edge extended X-ray absorption fine structure (EXAFS) fitting of $La_{0.9}K_{0.1}Al_{1-y}Mn_yO_{3-\delta}$ perovskite supports. Top graphs display a comparison of data (black) and fit (red) of the magnitude of the Fourier transform of the EXAFS χ data. Bottom graphs display a comparison of data (black) and fit (red) of the k^3 weighted data. (a) $La_{0.9}K_{0.1}Al_{0.4}Mn_{0.6}O_{3-\delta}$ pre-reduced; (b) $La_{0.9}K_{0.1}AlO_{3-\delta}$ pre-reduced.

When potassium nitrate is impregnated onto the $LaAlO_{3-\delta}$ perovskite, needle-like structures of potassium and aluminium-enriched areas were observed (Supporting Information Figure S3b). Potentially, the colocation of potassium and aluminium could indicate the formation of $KAlO_2$. However, as the phase is unstable in the presence of CO_2 or moisture, it would phase-separate into an amorphous aluminium oxide and potassium carbonate in air and/or under FT synthesis.[19] The only sample showing similar structures, albeit much smaller in size, is $La_{0.9}K_{0.1}AlO_{3-\delta}$ before reduction (Supporting Information Figure S3b). The K and Mn K-edge X-ray absorption near edge structure (XANES) of the samples as-synthesised and after exposure to a stream of hydrogen at 450 °C were analysed, simulating the activation procedure of the FT catalyst (Figure 1b,c, Supporting Information Figures S4 and S5). Mn K-edge spectra prior and post reduction correspond to $LaMnO_3$.[20,21] Based on the E_0 position, the oxidation state of Mn in the K-doped perovskites prior to reduction was higher than that in $LaMnO_3$, to compensate for the reduced average A site charge. Reduction resulted in a change in Mn-oxidation state from 3.5 to 3.2 while retaining the features of a perovskite. In concurrence with XRD and XANES, EXAFS analysis demonstrated that the Mn environment in all samples, prior and post reduction, corresponds to that expected for a perovskite (Table 1 and Supporting Information Figure S4).

Given the concentration of the K dopant, evidence for the inclusion of K within the structure cannot be deduced from the Mn edge data. Therefore, potassium K-edge XANES and

https://doi.org/10.1021/acscatal.3c00924
ACS Catal. 2023, 13, 6862−6872

Table 2. Potassium K-Edge EXAFS Fitting Values for $La_{0.9}K_{0.1}Al_{1-y}Mn_yO_{3-\delta}$ Perovskite Supports[a]

sample	scattering path	coordination number[b]	$2\sigma^2$ (Å^2)	R (Å)	delr	E_f (eV)	R_{factor}, reduced χ^2[e]
KCl	K−Cl	6	0.021(3)	3.12(2)	−0.02(2)	−3(1)	0.012 (473.6)
	K−K	12	0.031(4)	4.4(3)	0.04(3)		
K_2CO_3	K−O	7.5	0.0251(9)	2.79(2)	−0.06(2)	5(1)	0.0050 (220.1)
	K−K	2.5	0.015(1)	3.70(2)	0.18(2)		
$La_{0.9}K_{0.1}Al_{0.4}Mn_{0.6}O_{3-\delta}$ pre-reduced	K−O 1.1	3	0.020(5)	2.60(3)	0.10(3)	−0.386[c]	0.0072 (165.1)
	K−O 1.2	5		2.78(2)	−0.02(2)		
	K−O 1.3	3		3.37(5)	0.26(5)		
	K−Mn	8	0.05(2)	3.69(7)	0.26(7)		
	K−La	6	0.023(8)	4.28(5)	0.32(5)		
	K−O 1.4	12	0.016(6)	5.23(4)	0.013(97)		
	K−O 1.5	6	0.020(16)	4.8(1)	0.36(4)		
$La_{0.9}K_{0.1}AlO_{3-\delta}$ pre-reduced	K−O 1.1	3	0.020(6)	2.85(6)	0.35(6)	0.829[c]	0.0063 (172.3)
	K−O 1.2	5		2.69(2)	−0.11(2)		
	K−O 1.3	3		3.45(5)	0.34(5)		
	K−Al	8	0.04(1)	3.89(7)	0.62(7)		
	K−La	6	0.025(8)	4.27(4)	0.31(4)		
	K−O 1.4	12	0.021(7)	5.22(3)	0.35(3)		
	K−O 1.5	6	0.0198[d]	4.77(8)	−0.06(8)		

[a]Fixed parameters: S_o^2 = 1.002 calculated from KCl standard. [b]Coordination number fixed. [c]Fixed energy shift. [d]Fixed $2\sigma^2$ from $La_{0.9}K_{0.1}Al_{0.4}Mn_{0.6}O_3$ fit. [e]Value given in brackets.

EXAFS analyses were performed to understand the local structure of K. Fingerprinting of the reduced $La_{0.9}K_{0.1}Al_{1-y}Mn_yO_{3-\delta}$ spectra against a database of K standards (Figure 1c and Supporting Information Figure S5), including KOH, $KHCO_3$, and K_2CO_3 (which are reported for conventionally prepared promoted catalysts[11,22]), demonstrates that K is not present as a phase-separated structure. $KAlO_2$ can be discounted given its instability in the presence of moisture or CO_2. Only the XANES of unreduced $La_{0.9}K_{0.1}AlO_{3-\delta}$ showed any indication of K_2CO_3. In comparison, the $LaAlO_{3-\delta}$ perovskite impregnated with potassium nitrate shows a clear potassium K-edge spectrum of KNO_3, which converted to K_2CO_3 after reductive treatment (Supporting Information Figure S5b). XPS and ISS surface analyses were employed to further probe potential surface segregation of potassium species (Figure 1e,f). XPS showed an elevated K/La ratio (Supporting Information Table S2), marginally above that anticipated from elemental analysis, though sample probing depth must be accounted for in these systems given that the particles are in a similar size regime to the information depth of photoemission from Al Kα X-rays and at the mercy of topological influences. Both as-prepared and pre-reduced $La_{0.9}K_{0.1}AlO_{3-\delta}$ showed elevated surface K content, above that found for the $La_{0.9}K_{0.1}Al_{1-y}Mn_yO_{3-\delta}$ samples, though reductive treatment reduced this apparent surface enrichment. ISS analysis, however, indicated that the outer surface composition is much closer to that expected for a homogeneous perovskite. The difference to the targeted K/La ratio of 0.1 is likely a result of potassium removal by sputtering. This indicates that K enrichment seen using XPS is indeed primarily due to topological effects. Unreduced $La_{0.9}K_{0.1}AlO_{3-\delta}$ retained a high K content at the surface, suggesting some phase segregation, which disappeared after reduction.

Comparison of the EXAFS wavelet transformations of the perovskite supports and K_2CO_3 reference shows clear differences in R space above 3 Å (Figure 1c and Supporting Information Figure S6). Fitting of the data (excluding $La_{0.9}K_{0.1}AlO_{3-\delta}$, which has K_2CO_3 phase impurities in the unreduced state) shows that the larger and lower charge K^+ cation (relative to La^{3+}) is accommodated into the perovskite structure through an asymmetric expansion of the first shell oxygen environment (Figure 2 and Table 2 and Supporting Information Figure S7). The model indicates expansion of the 6 K−O bonds within the plane, but no expansion of those above or below the plane (Figure 3). Furthermore, the anticipated over-bonding of the site is alleviated by a reduction in the first shell coordination number from 12 to 11. Such oxygen nonstoichiometry is essential for K incorporation into $LaAlO_{3-\delta}$, as neither La nor Al cations can accommodate the charge differential as Mn can. This also explains the absence of a shift in lattice parameters when only K is incorporated into the perovskite lattice. The presence of K_2CO_3 in the unreduced $La_{0.9}K_{0.1}AlO_{3-\delta}$, as seen by XANES and the

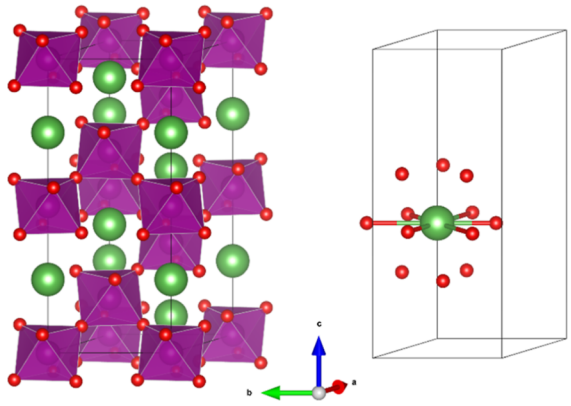

Figure 3. Three-dimensional representation[23] of the rhombohedral $LaMnO_3$[24] unit cell. Large spheres represent La^{3+} and small spheres located on the corners of the octahedra represent O^{2-}. Mn^{3+} is located in the centre of the octahedra. The left image displays the full unit cell, while the right image highlights the 12 O^{2-} coordinated with the La^{3+} cation, with the 6 O^{2-} in the a−b plane expanding/contracting with substitution of the lanthanum site. Upon substitution of La^{3+} with K^+, extended X-ray absorption fine structure modelling suggests that one O^{2-} above or below the a−b plane is removed resulting in a reduction of the coordination number from 12 to 11.

https://doi.org/10.1021/acscatal.3c00924
ACS Catal. 2023, 13, 6862−6872

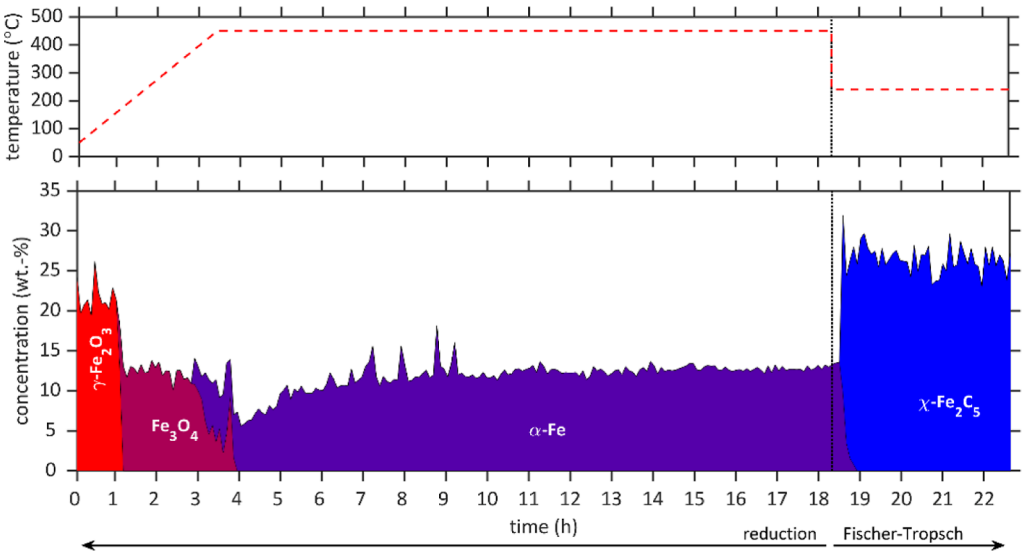

Figure 4. In situ X-ray diffraction characterization of Fe nanoparticles supported on $La_{0.9}K_{0.1}AlO_{3-\delta}$. Crystalline phase quantification area plot of $Fe/La_{0.9}K_{0.1}AlO_{3-\delta}$ as a function of time on stream as obtained *via* Rietveld refinement. The top panel displays the sample temperature and the bottom panel the concentration of the iron-containing phases as a function of time on stream. The samples were heated in a continuous flow of H_2 at atmospheric pressure (40 $mL{\cdot}min^{-1}{\cdot}g_{catalyst}^{-1}$) from 50 to 450 °C at 2 °C/min and held for 15 h (total reduction time 18.033 h). Subsequently, the reactor temperature was reduced to 240 °C, the pressure increased to 13.5 bar, and the catalyst exposed for 4.17 h to a stream of H_2 and CO in a 2:1 ratio as a pace velocity of 383 $mL{\cdot}min^{-1}{\cdot}g_{catalyst}^{-1}$.

wavelet-transformed EXAFS data, can be explained by the lack of sufficient oxygen nonstoichiometry, which is then remedied by the reduction at 450 °C, an observation further supported by a concomitant reduction in carbon species at 289 eV in the XPS analysis (carbonates/adsorbed CO_2) by approximately 25% following reduction (Figure 1e/Supporting Information Table S2) (Figure 4).

Further evidence that K is located within the perovskite lattice is provided by the successful fitting of the first shell K−La, K−Mn(Al) and second shell K−O paths (Figure 2, Table 2 and Supporting Information Figure S7). To confirm the validity of the model, paths representative of KOH, K_2O, and K_2CO_3 were separately fitted to the data but resulted in unrealistic parameters and poor fits (Supporting Information Figures S7−S9 and Table S3). This confirms that K has been incorporated into the perovskite lattice of all reduced perovskite supports studied.

Maghemite (γ-Fe_2O_3) nanoparticles were prepared *via* precipitation from an iron(II) chloride precursor solution[25] and subsequently deposited onto the supports with an ultrasound-induced physical mixing technique[26] targeting a maghemite loading of 20 wt % (Figure 3; Supporting Information Table S1; Figure S10). The supported catalysts are termed $Fe\text{-}La_{1-x}K_xAl_{1-y}Mn_yO_{3-\delta}$. The average oxidic crystallite size is 22 nm (Figure 1d), significantly above the size range for the activated metallic and carbide iron species, associated with crystallite size-dependent changes in activity and selectivity in the FT synthesis.[27,28]

The reduction and formation behaviour of the supported γ-Fe_2O_3 nanoparticles was studied in an in-house developed in situ XRD capillary cell[16] (Figure 3, Supporting Information Figures S11 and S12). On the $LaAlO_{3-\delta}$ carrier, the maghemite phase is rapidly converted to magnetite (Fe_3O_4) in a hydrogen atmosphere at 260 °C before fully reducing to the metallic α-Fe from 400 °C onward. The addition of K to the perovskite structure lowers the reduction temperature of the maghemite to magnetite by 80 °C without affecting the reduction of magnetite to the metallic iron. This is in line with our previous observations, showing that potassium promotion of iron catalysts influences the reduction temperature to Fe_3O_4 but not to α-Fe.[29] In the presence of an additional substitution of Al with Mn in the B site, the enhancement of the first reduction step is not observed. Based on the XANES spectra of the potassium K-edge discussed earlier, it is likely that the facilitation of the first reduction step is a result of free K_2CO_3 which is only incorporated into the Mn-free perovskite structure upon the reduction-induced oxygen nonstoichiometry.

Following the reductive treatment, the catalysts were exposed to FT conditions for approximately 4 h to monitor the carburization process. On the unmodified perovskite support, Hägg carbide (χ-Fe_2C_5) formation is observed after 1.3 h and all metallic iron reflexes disappear after 1.8 h. When K is present in the perovskite structure, this process is significantly enhanced with the first evidence of carbide recorded after just 0.25 h and full conversion of the metallic phase after 0.5 h. The enhancement of the carburization process through K has been reported extensively for classic promotion and is rationalised by a donation of electron density from the alkali metal to the iron phase, enhancing CO adsorption over H_2 adsorption and weakening the carbon−oxygen bond.[2,30] The observed effect on carburization is therefore direct evidence that K incorporated in a perovskite structure does provide promotional activity to a catalytically active phase. The additional presence of Mn does not influence this phase transition on bulk scale. Effects on the detailed composition of the carbide phase cannot be excluded at this stage.

All catalysts were studied for their FT performance in a 600 mL slurry CSTR reactor. The unmodified $Fe\text{-}LaAlO_{3-\delta}$ compares well with more classical supports such as SiO_2, Al_2O_3, ZrO_2, and TiO_2, both with regard to CO conversion as well as product selectivity (Supporting Information Figure S13 and Table S4). A 10 at. % replacement of La with K increases

https://doi.org/10.1021/acscatal.3c00924
ACS Catal. 2023, 13, 6862−6872

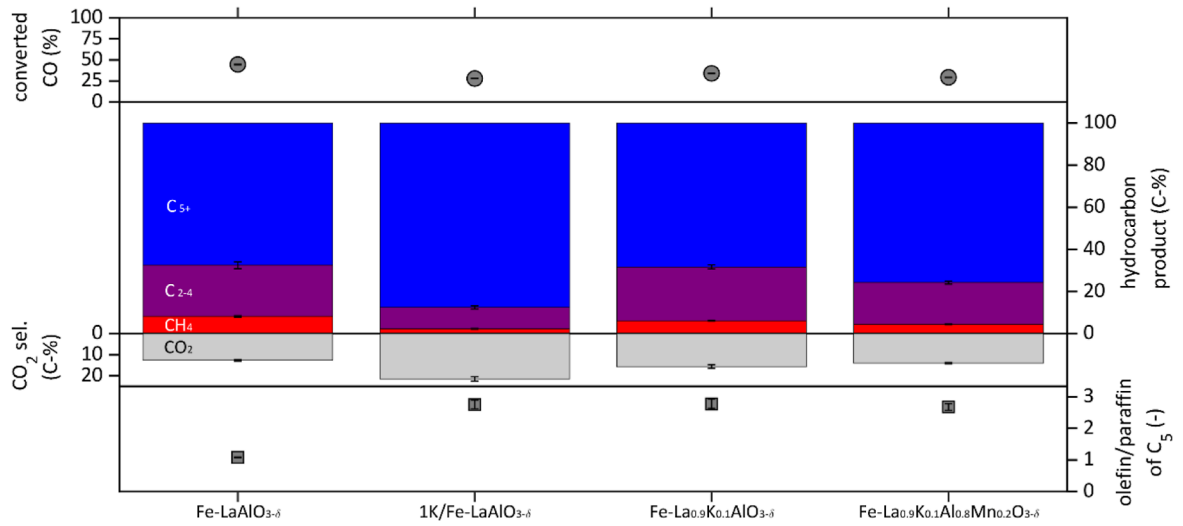

Figure 5. Catalyst performance under Fischer−Tropsch (FT) reaction conditions. The top panel displays the CO conversion of iron supported on $LaAlO_{3-\delta}$, supported on $LaAlO_{3-\delta}$, and promoted with 1 wt % potassium *via* impregnation (1 K/Fe-$LaAlO_{3-\delta}$), and iron supported on $La_{0.9}K_{0.1}Al_{1-y}Mn_yO_{3-\delta}$ with y = 0, 0.2. For all samples with K present, the space velocity was elevated by a factor of 3.75 to achieve comparable conversion levels. The stacked bar chart in the middle of the figure represents the composition (CH_4, C_{2-4}, and C_{5+}) of the hydrocarbon fraction in the product stream as well as the selectivity toward CO_2 of the same catalysts. In the bottom panel, the ratio of primary olefins to linear paraffins in the C_5 hydrocarbon faction is shown. Error bars are provided for all datasets. All FT experiments were carried out in a 600 mL slurry CSTR reactor at 240 °C, 15 bar pressure, a H_2/CO ratio of 2 with 10 vol % N_2 as internal standard, and a space velocity of 8 $mL{\cdot}min^{-1}{\cdot}g_{catalyst}^{-1}$ for Fe-$LaAlO_3$ and 30 $mL{\cdot}min^{-1}{\cdot}g_{catalyst}^{-1}$ for the K-containing catalysts. Data collected after 48 h time on stream.

the CO conversion from 45 to 76% which equates a rate increase per mol iron in the reactor of 1.6 (Supporting Information Table S4). This increase is paralleled by a nine percentage points increase in chain growth probability and an almost fourfold increase in CO_2 selectivity. The increased chain growth materialises predominantly in the short chain hydrocarbon fraction with an overall increased olefinicity, that is, an increased ratio of primary olefin to n-paraffin concentration. For a realistic comparison of catalyst selectivity, the K-bearing catalyst was re-evaluated at a 3.75 times higher space velocity, resulting in a CO conversion of 34% (Figure 5). At this near iso-conversion condition, the CO_2 selectivity is only slightly enhanced (12.7 vs 15.6 C %) at an even further increased chain growth probability (12% points increase compared to the Fe-$LaAlO_{3-\delta}$ catalyst), resulting in a reduction of methane and an increase in higher hydrocarbon concentrations in the product stream. The olefinicity remains elevated. The additional substitution of 20 at. % of Al with Mn retains the enhanced activity and results in a further increased chain growth probability, a reduced methane selectivity, and significantly increased C_{5+} selectivity. Furthermore, CO_2 formation is suppressed by the presence of Mn. Higher concentrations of Mn, both in the presence and absence of K, reduce the activity to levels below the unpromoted sample, combined with increased WGS activity and FT chain growth probability (Supporting Information Figure S13c−f).

To contextualize the enhanced performance of the potassium-containing perovskites, $LaAlO_{3-\delta}$ was impregnated with 2, 1, or 0.5 wt % K before the deposition of the maghemite nanoparticles. 2 wt % equates the total potassium concentration in the perovskites with a 10 at. % replacement of La with K. However, the resulting surface concentration is much higher in the impregnated sample. Of the three catalysts, the two lower promoter concentrations yield an elevated CO conversion (76 and 78%; Supporting Information Figure S13c,d) comparable to the enhancement observed for the potassium-containing perovskite samples. Compared to Fe-$La_{0.9}K_{0.1}AlO_{3-\delta}$ and Fe-$La_{0.9}K_{0.1}Al_{0.8}Mn_{0.2}O_{3-\delta}$ at an elevated space velocity, that is, at conversion levels also comparable with the unpromoted catalyst, the hydrocarbon product slate is slightly heavier, due to a lower C_1−C_4 fraction (Figure 5.). However, the CO_2 selectivity is up to 60% higher for the impregnated samples due to a parallel promotion of the WGS activity, resulting in an overall higher undesired C_1 product stream.

By anchoring potassium within the perovskite matrix, we have been able to deconvolute its enhancement of the FT and WGS activity. The potassium-containing perovskites yield less CO_2 at equivalently enhanced CO conversion rates. Traditionally, the WGS reaction is beneficial when operating large-scale FT plants with a H_2 lean feedstock, for example, as obtained from the gasification of coal. In a future scenario of small-scale power-to-liquid plants, the suppression of the WGS activity provides the opportunity to employ a low-cost iron-based FT catalyst instead of their cobalt-based counterparts, without loss of product quality. The developed promoter presentation further overcomes promoter mobility, especially at the expected harsh power-to-liquid reaction conditions.

After 48 h at FT conditions, the spent catalysts were recovered in solidified wax. Fragments of the wax-covered catalyst were digested for elemental analysis (Supporting Information Table S5). No significant change in composition was detected. To prepare the samples for XRD, wax residues were removed *via* Soxhlet extraction in xylene at 140 °C for 4 days. The obtained diffraction patterns show a stable perovskite structure (Supporting Information Figure S14). In the presence of potassium, the iron phase is predominantly carbide with minor traces of magnetite. However, in the absence of the alkali, about 6 wt % of metallic iron is detected in the catalyst alongside the Hägg carbide and traces of Fe_3O_4. The speciation of potassium does not change after 48 h under reaction conditions (Supporting Information Figure S15).

https://doi.org/10.1021/acscatal.3c00924
ACS Catal. 2023, 13, 6862−6872

CONCLUSIONS

We have synthesised new support materials by anchoring promoting elements within a perovskite lattice. We demonstrated that these novel materials can act as empowered catalyst supports by providing both the physical functionality of common catalyst support materials as well as the chemical and electronic effects of conventional promoters. Due to the versatility of perovskites, it is expected that improved promoter incorporation can be achieved by changing the composition of the parent perovskite.[31] While the materials in the present study displayed low specific surface areas, a number of synthesis techniques using templating approaches have been reported to overcome this perovskite-specific limitation.[32,33] In the case of the iron-based FT synthesis, this new approach has outperformed conventional techniques by matching conversion enhancements of conventional promotion while promoting the FT reaction more selectively over the WGS reaction. These enhancements were stable over the evaluation period of 48 h. There is no reason to assume that the observed effects represent a singularity regarding the promoter elements and the chosen reaction. We expect that the underlying design principles can be transferred to other catalytic processes breaking the boundaries of known performance enhancement abilities of promoter elements.

ASSOCIATED CONTENT

Supporting Information

The Supporting Information is available free of charge at https://pubs.acs.org/doi/10.1021/acscatal.3c00924.

Elemental composition of synthesised perovskite materials and γ-Fe_2O_3 loading on catalyst precursors; XRD characterization of synthesised $La_{1-x}K_xAl_{1-y}Mn_yO_{3-\delta}$ perovskites; STEM bright-field micrograph of $La_{0.9}K_{0.1}Al_{0.4}Mn_{0.2}O_{3-\delta}$ after reductive pre-treatment and individual EDS maps of constituting elements; HAADF STEM micrograph after reductive treatment and individual EDS maps of constituting elements; Manganese K-edge EXAFS fitting of $La_{0.9}K_{0.1}Al_{1-y}Mn_yO_{3-\delta}$ perovskites; XANES of the potassium K-edge; surface elemental composition of $LaAlO_{3-\delta}$, $La_{0.9}K_{0.1}Al_{0.4}Mn_{0.6}O_{3-\delta}$, and $La_{0.9}K_{0.1}AlO_{3-\delta}$ determined by XPS; wavelet transformation of k^1 data from potassium K-edge EXAFS; potassium K-edge EXAFS fitting of K_2CO_3 and KCl standards; fitting of the potassium K-edge EXAFS spectra of pre-reduced $La_{0.9}K_{0.1}Al_{0.4}Mn_{0.6}O_{3-\delta}$ perovskite supports with KCO_3 model; fitting of the potassium K-edge EXAFS spectra of pre-reduced $La_{0.9}K_{0.1}Al_{0.4}Mn_{0.6}O_{3-\delta}$ perovskite supports with KOH or K_2O model; potassium K-edge EXAFS fitting values for pre-reduced $La_{0.9}K_{0.1}Al_{0.4}Mn_{0.6}O_{3-\delta}$ fitted with KCO_3 model and vice versa; XRD characterization of synthesised γ-Fe_2O_3 nanoparticles; In situ XRD of synthesised catalysts during reduction and FT synthesis; quantification of in situ XRD characterization during reduction and FT synthesis; catalyst performance under FT reaction conditions; CO conversion and selectivity of all tested catalysts; elemental composition of perovskite in the spent catalyst; XRD characterization of spent catalysts; XRD patterns of Fe-$LaAlO_{3-\delta}$ and Fe-$La_{0.9}K_{0.1}Al_{0.8}Mn_{0.2}O_{3-\delta}$ after 48 h TOS under FT conditions and extracted from solidified wax *via* Soxhlet extraction; and XAS of the potassium K-edge of spent catalysts (PDF)

AUTHOR INFORMATION

Corresponding Author

Nico Fischer − *DSI-NRF Centre of Excellence in Catalysis c*change and Catalysis Institute, Department of Chemical Engineering, University of Cape Town, Rondebosch, Cape Town 7701, South Africa;* orcid.org/0000-0002-8817-3621; Email: nico.fischer@uct.ac.za

Authors

Motlokoa Khasu − *DSI-NRF Centre of Excellence in Catalysis c*change and Catalysis Institute, Department of Chemical Engineering, University of Cape Town, Rondebosch, Cape Town 7701, South Africa*

Wijnand Marquart − *DSI-NRF Centre of Excellence in Catalysis c*change and Catalysis Institute, Department of Chemical Engineering, University of Cape Town, Rondebosch, Cape Town 7701, South Africa;* orcid.org/0000-0002-7319-0090

Patricia J. Kooyman − *DSI-NRF Centre of Excellence in Catalysis c*change and Catalysis Institute, Department of Chemical Engineering, University of Cape Town, Rondebosch, Cape Town 7701, South Africa;* orcid.org/0000-0003-1252-5296

Charalampos Drivas − *HarwellXPS, Research Complex at Harwell, Didcot OX11 0FA, U.K.; Department of Chemical Engineering and Analytical Science, University of Manchester, Manchester M13 9PL, U.K.*

Mark A. Isaacs − *HarwellXPS, Research Complex at Harwell, Didcot OX11 0FA, U.K.; Department of Chemistry, University College London, London WC1H 0AJ, U.K.;* orcid.org/0000-0002-0335-4272

Alexander J. Mayer − *Department of Chemistry, Loughborough University, Loughborough LE11 3TU, U.K.*

Sandie E. Dann − *Department of Chemistry, Loughborough University, Loughborough LE11 3TU, U.K.*

Simon A. Kondrat − *Department of Chemistry, Loughborough University, Loughborough LE11 3TU, U.K.;* orcid.org/0000-0003-4972-693X

Michael Claeys − *DSI-NRF Centre of Excellence in Catalysis c*change and Catalysis Institute, Department of Chemical Engineering, University of Cape Town, Rondebosch, Cape Town 7701, South Africa;* orcid.org/0000-0002-5797-5023

Complete contact information is available at: https://pubs.acs.org/10.1021/acscatal.3c00924

Author Contributions

N.F. initiated and conceived the research; M.K. synthesised, characterised, and tested the catalysts; M.K., W.M., M.C., and N.F. analysed and interpreted the performance data; P.J.K. performed part of the TEM characterization; C.D. and M.A.I. performed XPS and ISS analyses and interpretation; A.J.M. and S.A.K. performed the XAS characterization; A.J.M., W.M., and S.A.K. performed the XAS data analysis; S.A.K., S.D., and N.F. contributed to data interpretation; and S.A.K. and N.F. wrote the manuscript. All authors contributed to the scientific discussion and edited the manuscript.

https://doi.org/10.1021/acscatal.3c00924
ACS Catal. 2023, 13, 6862−6872

Funding

Research supported by the DSI-NRF Centre of Excellence in Catalysis c*change grant under the Synthesis Gas Programme, by the University of Cape Town Faculty of Engineering and the Built Environment 2021 Block Grant, by the National Research Foundation of South Africa Grant (no. 94878), by the UK Catalysis Hub Block Allocation Group at the B18 beamline of the Diamond Light Source, and by the Royal Academy of Engineering Distinguished International Associate Programme (DIA-2021-119).

Notes

The authors declare no competing financial interest.

■ ACKNOWLEDGMENTS

The authors thank Dr Giannantonio Cibin from the B18 beamline of the Diamond Light Source for the support during the XAS data analysis. They thank the Centre for High Resolution Transmission Electron Microscopy at the Nelson Mandela University for access provided and their staff for their support. The X-ray photoelectron (XPS) data collection was performed at the EPSRC National Facility for XPS ("HarwellXPS"), operated by Cardiff University and UCL, under Contract no. PR16195.

■ REFERENCES

(1) Dry, M. E. The Fischer-Tropsch synthesis. In *Catalysis: Science and Technology*; Anderson, J. R., Ed.; Springer-Verlag: Berlin, Germany, 1981; Vol. *1*, pp 159−255.

(2) Dry, M. E.; Shingles, T.; vanBotha, H. C. S. Factors influencing the formation of carbon on iron Fischer-Tropsch catalysts: I. The influence of promoters. *J. Catal.* **1970**, *17*, 341−346.

(3) Anderson, R. B.; Seligman, B.; Shultz, J. F.; Kelly, R.; Elliott, M. A. Fischer-Tropsch synthesis. Some important variables of - the synthesis of iron catalysts. *Ind. Eng. Chem.* **1952**, *44*, 391−397.

(4) Connell, G.; Dumesic, J. A. Migration of potassium on iron and alumina surfaces as studied by Auger electron spectroscopy. *J. Catal.* **1985**, *92*, 17−24.

(5) Anderson, R. B. *The Fischer-Tropsch Synthesis*; Academic Press, 1984, p 301.

(6) Ngantsoue-Hoc, W.; Zhang, Y.; O'Brien, R. J.; Luo, M.; Davis, B. H. Fischer−Tropsch synthesis: activity and selectivity for Group I alkali promoted iron-based catalysts. *Appl. Catal., A* **2002**, *236*, 77−89.

(7) Bukur, D. B.; Mukesh, D.; Patel, S. A. Promoter effects on precipitated iron catalysts for Fischer-Tropsch synthesis. *Ind. Eng. Chem. Res.* **1990**, *29*, 194−204.

(8) Xu, L.; Wang, Q.; Xu, Y.; Huang, J. Promotion effect of K_2O and MnO additives on the selective production of light alkenes via syngas over Fe/silicalite-2 catalysts. *Catal. Lett.* **1995**, *31*, 253−266.

(9) Tao, Z.; Yang, Y.; Wan, H.; Li, T.; An, X.; Xiang, H.; Li, Y. Effect of manganese on a potassium-promoted iron-based Fischer-Tropsch synthesis catalyst. *Catal. Lett.* **2007**, *114*, 161−168.

(10) Dad, M.; Fredriksson, H. O. A.; Van de Loosdrecht, J.; Thüne, P. C.; Niemantsverdriet, J. W. Stabilization of iron by manganese promoters in uniform bimetallic FeMn Fischer−Tropsch model catalysts prepared from colloidal nanoparticles. *Catal., Struct. React.* **2015**, *1*, 101−109.

(11) Jacobs, G.; Pendyala, V. R. R.; Martinelli, M.; Shafer, W. D.; Gnanamani, M. K.; Khalid, S.; MacLennan, A.; Hu, Y.; Davis, B. H. Fischer−Tropsch Synthesis: XANES Spectra of Potassium in Promoted Precipitated Iron Catalysts as a Function of Time On-stream. *Catal. Lett.* **2017**, *147*, 1861−1870.

(12) Stencel, J. M.; Diehl, J. R.; Miller, S. R.; Anderson, R. A.; Zarochak, M. F.; Pennline, H. W. Iron/manganese oxide catalysts: surface specification and slurry -phase fischertropsch activity. *Appl. Catal.* **1987**, *33*, 129−143.

(13) Feltes, T. E.; Espinosa-Alonso, L.; Smit, E. d.; D'Souza, L.; Meyer, R. J.; Weckhuysen, B. M.; Regalbuto, J. R. Selective adsorption of manganese onto cobalt for optimized $Mn/Co/TiO_2$ Fischer−Tropsch catalysts. *J. Catal.* **2010**, *270*, 95−102.

(14) Megha, U.; Shijina, K.; Varghese, G.; LaCo, N. $_6Fe_{0.4}O_3$ perovskites synthesized by citrate sol gel auto combustion method. *Process. Appl. Ceram.* **2014**, *8*, 87−92.

(15) Ravel, B.; Newville, M. ATHENA, ARTEMIS, HEPHAESTUS: data analysis for X-ray absorption spectroscopy using IFEFFIT. *J. Synchrotron Radiat.* **2005**, *12*, 537−541.

(16) Fischer, N.; Claeys, M. Phase changes studied under in situ conditions—A novel cell. *Catal. Today* **2016**, *275*, 149−154.

(17) Rietveld, H. A profile refinement method for nuclear and magnetic structures. *J. Appl. Crystallogr.* **1969**, *2*, 65−71.

(18) Schulz, H.; Boehringer, W.; KohlRahman, C. N.; Will, A. Entwicklung und Anwendung der Kapillar-GC-Gesamtprobentechnick fuer Gas/Dampf-Vielstoffgemische. *DGMK Forschungsbericht* **1984**, *3*, 320−329.

(19) Sokolowski, J.; Kotarba, A. The Structure of Potassium Aluminium Oxide $KAlO_2$. *Mater. Sci. Forum* **2000**, *321−324*, 954−959.

(20) Celorrio, V.; Calvillo, L.; van den Bosch, C. A. M.; Granozzi, G.; Aguadero, A.; Russell, A. E.; Fermín, D. J. Mean Intrinsic Activity of Single Mn Sites at $LaMnO_3$ Nanoparticles Towards the Oxygen Reduction Reaction. *ChemElectroChem* **2018**, *5*, 3044−3051.

(21) Celorrio, V.; Calvillo, L.; Granozzi, G.; Russell, A. E.; Fermin, D. J. $AMnO_3$ (A = Sr, La, Ca, Y) Perovskite Oxides as Oxygen Reduction Electrocatalysts. *Top. Catal.* **2018**, *61*, 154−161.

(22) Davies, C. J.; Mayer, A.; Gabb, J.; Walls, J. M.; Degirmenci, V.; Thompson, P. B. J.; Cibin, G.; Golunski, S.; Kondrat, S. A. Operando potassium K-edge X-ray absorption spectroscopy: investigating potassium catalysts during soot oxidation. *Phys. Chem. Chem. Phys.* **2020**, *22*, 18976−18988.

(23) Momma, K.; Izumi, F. VESTA 3 for three-dimensional visualization of crystal, volumetric and morphology data. *J. Appl. Crystallogr.* **2011**, *44*, 1272−1276.

(24) Guo, Y.; Zhang, X.; Wäppling, R. Crystal structure of $La_{1-x}Sr_xMnO_{3-2x+\delta}F_{2x}$. *J. Alloys Compd.* **2000**, *306*, 133−140.

(25) Yang, X.-C.; Shang, Y.-L.; Li, Y.-H.; Zhai, J.; Foster, N. R.; Li, Y.-X.; Zou, D.; Pu, Y. Synthesis of Monodisperse Iron Oxide Nanoparticles without Surfactants. *J. Nanomater.* **2014**, *2014*, 740856−740860.

(26) Fischer, N.; van Steen, E.; Claeys, M. Preparation of supported nano-sized cobalt oxide and fcc cobalt crystallites. *Catal. Today* **2011**, *171*, 174−179.

(27) Fischer, N.; van Steen, E.; Claeys, M. Structure sensitivity of the Fischer−Tropsch activity and selectivity on alumina supported cobalt catalysts. *J. Catal.* **2013**, *299*, 67−80.

(28) Torres Galvis, H. M.; Bitter, J. H.; Davidian, T.; Ruitenbeek, M.; Dugulan, A. I.; de Jong, K. P. Iron Particle Size Effects for Direct Production of Lower Olefins from Synthesis Gas. *J. Am. Chem. Soc.* **2012**, *134*, 16207−16215.

(29) Fischer, N.; Henkel, R.; Hettel, B.; Iglesias, M.; Schaub, G.; Claeys, M. Hydrocarbons via CO_2 Hydrogenation Over Iron Catalysts: The Effect of Potassium on Structure and Performance. *Catal. Lett.* **2016**, *146*, 509−517.

(30) Dry, M. E.; Shingles, T.; Boshoff, L. J.; Oosthuizen, G. J. Heats of chemisorption on promoted iron surfaces and the role of alkali in Fischer-Tropsch synthesis. *J. Catal.* **1969**, *15*, 190−199.

(31) Bradha, M.; Hussain, S.; Chakravarty, S.; Amarendra, G.; Ashok, A. Synthesis, structure and total conductivity of A-site doped $LaTiO_{3-\delta}$ perovskites. *J. Alloys Compd.* **2015**, *626*, 245−251.

(32) de Lima, R.; Batista, M. S.; Wallau, M.; Sanches, E. A.; Mascarenhas, Y. P.; Urquieta-González, E. A. High specific surface area LaFeCo perovskites—Synthesis by nanocasting and catalytic behavior in the reduction of NO with CO. *Appl. Catal., B* **2009**, *90*, 441−450.

(33) Wang, Y.; Ren, J.; Wang, Y.; Zhang, F.; Liu, X.; Guo, Y.; Lu, G. Nanocasted Synthesis of Mesoporous $LaCoO_3$ Perovskite with

https://doi.org/10.1021/acscatal.3c00924
ACS Catal. 2023, 13, 6862−6872

Extremely High Surface Area and Excellent Activity in Methane Combustion. *J. Phys. Chem. C* **2008**, *112*, 15293−15298.

https://doi.org/10.1021/acscatal.3c00924
ACS Catal. 2023, 13, 6862−6872